

Mechanical behavior and phase change of alkali-silica reaction products under hydrostatic compression

Guoqing Geng,^{a,b,*} Zhenguo Shi,^c Andreas Leemann,^c Konstantin Glazyrin,^d Annette Kleppe,^e Dominik Daisenberger,^e Sergey Churakov,^{a,f} Barbara Lothenbach,^{c,g} Erich Wieland^a and Rainer Dähn^a

Received 27 August 2019

Accepted 24 June 2020

Edited by C. M. Reddy, IISER Kolkata, India

Keywords: alkali-silica-reaction; high-pressure X-ray diffraction; mechanical property; phase change.

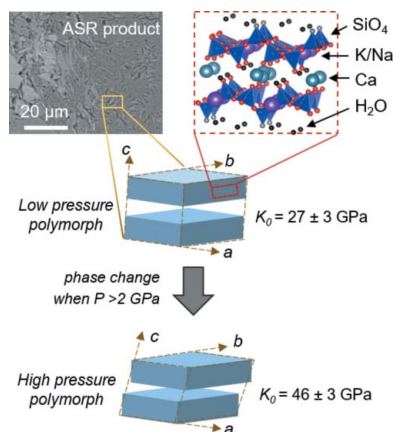
Supporting information: this article has supporting information at journals.iucr.org/b

^aLaboratory of Waste Management, Paul Scherrer Institut, OHLD/004, Villigen, Aargau 5232, Switzerland, ^bDepartment of Civil and Environmental Engineering, National University of Singapore, 117576, Singapore, ^cLaboratory for Concrete and Construction Chemistry, Swiss Federal Laboratories for Materials Science and Technology (Empa), Dübendorf, 8600, Switzerland, ^dPhoton Sciences, Deutsches Elektronen-Synchrotron (DESY), Hamburg, D-22603, Germany, ^eDiamond Light Source, Harwell Science and Innovation Campus, Fermi Ave, Didcot, OX11 0DE, United Kingdom, ^fInstitute of Geological Sciences, University of Bern, Switzerland, and ^gDepartment of Structural Engineering, Norwegian University of Science and Technology, Trondheim, 7491, Norway. *Correspondence e-mail: ceegg@nus.edu.sg

Alkali-silica reaction (ASR) causes severe degradation of concrete. The mechanical property of the ASR product is fundamental to the multiscale modeling of concrete behavior over the long term. Despite years of study, there is a lack of consensus regarding the structure and elastic modulus of the ASR product. Here, ASR products from both degraded field infrastructures and laboratory synthesis were investigated using high-pressure X-ray diffraction. The results unveiled the multiphase and metastable nature of ASR products from the field. The dominant phase undergoes permanent phase change via collapsing of the interlayer region and in-planar glide of the main layer, under pressure >2 GPa. The bulk moduli of the low- and high-pressure polymorphs are 27 ± 3 and 46 ± 3 GPa, respectively. The laboratory-synthesized sample and the minor phase in the field samples undergo no changes of phase during compression. Their bulk moduli are 35 ± 2 and 76 ± 4 GPa, respectively. The results provide the first atomistic-scale measurement of the mechanical property of crystalline ASR products.

1. Introduction

Alkali-silica reaction (ASR) occurs between the concrete pore solution and the reactive siliceous component of the aggregate (Mehta & Monteiro, 2014). It is among the most common mechanisms that lead to severe concrete degradation during the service life of infrastructures. ASR is characterized by the significant expansion of concrete and the substantial presence of micro-cracks filled (or partially filled) with reaction products (Mehta & Monteiro, 2014; Fournier & Bérubé, 2000). These reaction products are highly variable in chemical composition, atomistic structure and nano-morphology, depending on the microscale location of the product and the mineralogical/chemical boundary conditions of the aggregate and cement (Rajabipour *et al.*, 2015; Leemann *et al.*, 2011; Fernández-Jiménez & Puertas, 2002; De Ceukelaire, 1991; Shi *et al.*, 2015). For instance, the product veins inside reacted aggregates are often filled with crystalline products with nanoplate morphology, whereas featureless gel products often populate the veins outside the boundary of aggregates (Leemann, 2017; Cole *et al.*, 1981; Peterson *et al.*, 2006). The ASR products generally bear the composition of $(\text{CaO})_m \cdot (\text{Na/KO}_{0.5})_n \cdot (\text{SiO}_2) \cdot (\text{H}_2\text{O})_l$, where m and n range from 0.2 to 0.3 for



© 2020 International Union of Crystallography

the crystalline ASR product. For amorphous product, m has a larger variation range between 0.3 and 0.6 (Leemann & Lura, 2013; Katayama, 2012; Thomas, 2001; Geng *et al.*, 2020). Little is known regarding the water content in ASR product from affected infrastructures.

The substantial variation in the crystallinity of the ASR product has not been sufficiently discussed in early and even recent studies (Prezzi *et al.*, 1997; Hou *et al.*, 2004). Yet increasing micro-morphological (Leemann, 2017; Cole *et al.*, 1981; Katayama, 2012) and crystal-chemical (Leemann, 2017; Dähn *et al.*, 2016) studies have suggested the relevance of addressing this heterogeneity in order to realistically describe the physiochemical process of ASR at microscale. Recently, integrated investigations on field-extracted (Geng *et al.*, 2020) and laboratory-synthesized (Shi *et al.*, 2019, 2020) ASR samples provided new insight to the atomistic configuration of ASR products. As illustrated in Fig. 1, the crystalline ASR product was resolved to have a layer-silicate structure which is highly comparable to the mineral shlykovite (Geng *et al.*, 2020; Shi *et al.*, 2019; Pekov *et al.*, 2010). In each main layer, a sheet of Ca is charge balanced by two silicate sheets where K (and Na) ions are hosted in eight-membered silicate rings. The interlayer is populated with water. Despite the similarity of the main layer structure, the ASR product may exhibit variation in the basal spacing (*i.e.* the thickness of interlayer), resulting in multiple basal peaks in the micro-XRD of the ASR products (Geng *et al.*, 2020). The unit-cell angles α and β may also undergo variations suggesting an in-planar glide between adjacent layers. Meanwhile, the amorphous ASR product near the aggregate surface seems to possess a chemical environment similar to that of calcium silica hydrate (C-S-H) (Geng *et al.*, 2020). Therefore, one may expect the crystalline and amorphous ASR products to possess distinct physical properties, *e.g.* mechanical properties and water-uptake behavior.

To model the micro-mechanical process of ASR, it is essential to know the mechanical properties of the two distinct types of ASR product (Iskhakov *et al.*, 2018). Nano-indentation has been used to study the elastic modulus of the crystalline product (Leemann & Lura, 2013; Zhang *et al.*, 2017; Hu *et al.*, 2018). Leemann & Lura (2013) reported an elastic modulus of 7–9 GPa when reaching an indentation depth of $\sim 2\ \mu\text{m}$. At the same indentation depth, Zhang *et al.* (2017) reported a slightly higher elastic modulus ($\sim 14\ \text{GPa}$), whereas a much larger modulus ($\sim 65\ \text{GPa}$) at an indentation depth of $\sim 0.5\ \mu\text{m}$. Hu *et al.* (2018) reported an average elastic modulus of $\sim 27\ \text{GPa}$. The vast deviation suggests that the interaction

between the indent tip and the crystalline ASR product may involve a scaling effect, even at the dimension of a few microns. A similar scaling effect has been confirmed in the nano-indentation measurements of C-S-H which also contains nano-porosity (Hu *et al.*, 2019; Constantinides & Ulm, 2007; Geng *et al.*, 2017b). Ca-free gels extruded to the surface of the Furnas Dam (Brazil) were studied by high-pressure X-ray diffraction (HP-XRD) (Moon *et al.*, 2013) and nano-indentation (Johnson *et al.*, 2017), resulting in elastic moduli between 25 and 30 GPa. Yet these amorphous gels are distinct from crystalline ASR products in both chemical compositions and structural order. The intrinsic mechanical property of the crystalline ASR product remains largely unclear. In particular, the crystalline ASR product veins are proved to contain multiple phases with similar layer structure but a different stacking pattern. The difference in their mechanical property awaits investigation.

HP-XRD has been proven a robust method to probe the anisotropic mechanical property of macro-crystalline (Geng *et al.*, 2018a; Moon *et al.*, 2012; Comboni *et al.*, 2019) and nano-crystalline (Geng *et al.*, 2017a,b; Zhou *et al.*, 2019) phases in cementitious systems. Using a diamond-anvil-cell (DAC), hydrostatic pressure up to several hundred GPa can be applied to samples and the accompanied change of lattice parameters tracked by investigating the XRD pattern at elevated pressure (Mao *et al.*, 1986). An unambiguous correlation between unit-cell geometry and applied pressure is thus obtained, which is further used to solve the elastic properties. In this study, crystalline ASR products collected from the field, as well as synthesized in laboratory, were investigated using HP-XRD. Multiple phases with different lattice parameters were identified from these field samples. Their anisotropic mechanical properties and pressure-induced phase change were identified. The results provide novel insight into the behavior of crystalline ASR products under compression.

2. Methodology

2.1. Materials

HP-XRD studies possess the advantage of requiring a minimal volume of sample. This enables investigation of the real ASR products extracted from affected concrete, whose quantity is usually insufficient for other types of diffraction study. In order to study ASR products from different concrete specimens, here we selected three powder samples of crystalline ASR products from different field sources. Following the notation in our previous work (Geng *et al.*, 2020), Mels_pore was extracted from a porous space in the hardened cement paste near an aggregate surface inside an affected concrete bridge in Mels (Switzerland). ES1_agg and ES1_pore were extracted from inside an aggregate and from a porous space, respectively, from a laboratory-produced concrete cube exposed for 14 years to natural conditions in Valencia (Spain). Following the extraction, the samples were immediately sealed in plastic vials until usage in synchrotron experiments. There was no intended control of the relative humidity inside the

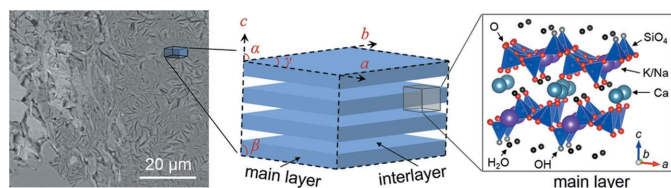


Figure 1

The layer-silicate structure of the crystalline ASR product from affected concrete. The micro-morphology image of a product vein is adopted from Geng *et al.* (2020).

plastic vials. These extracted samples do not contain aggregate impurities as demonstrated by the XRD data.

A laboratory-synthesized shlykovite, denoted as SKC, was also studied. It was produced by mixing SiO_2 , CaO and $(\text{Na}/\text{K})\text{OH}$ in a molar ratio of 1:0.25:0.5 and at a water-to-solid ratio of about 7:1. Following an 80-day curing at 80°C , the solid was filtered, dried and sealed in plastic vials until use. More details of SKC synthesis and characterization are given by Geng *et al.* (2020), Shi & Lothenbach (2019) and Shi *et al.* (2019).

2.2. High-pressure X-ray diffraction

HP-XRD studies of the field samples (Mels_pore, ES1_pore, ES1_agg) were conducted at beamline P02.2 of the Deutsches Elektronen-Synchrotron (Hamburg, Germany). The incident beam was focused to $8\ \mu\text{m} \times 3\ \mu\text{m}$, with an energy of 25.45 keV (wavelength $\lambda = 0.4872\ \text{\AA}$). Raw diffraction images were recorded with a PE-XRD1621 image plate. The laboratory sample SKC was studied at beamline I15 of the Diamond Light Source (Oxfordshire, UK). The incident beam, with an energy of 29.2 keV ($\lambda = 0.4246\ \text{\AA}$), was focused to $\sim 70\ \mu\text{m}$ to maximize the signal. A MAR345 image plate was used to collect the raw diffraction images.

The sample powders were loaded in cylindrical chambers, with diameters of 150–200 μm and depths of 70–90 μm , created by drilling stainless-steel gaskets. A Le Toullec type membrane DAC and a Mao-Bell type DAC were used in the beamtime in Diamond Light Source and DESY, respectively. Diamonds with culet diameter of 300–400 μm were used. A solution of ethanol and methanol (volume ratio 4:1) was used as pressure medium. The CeO_2 standard was measured in both beamlines to calibrate the center of the beam on the detector and the sample-to-detector distance. Hydrostatic pressure was applied from ambient (no applied pressure) to $\sim 8\ \text{GPa}$, at a step size of 1–2 GPa, followed by a complete unloading of the DAC. Due to the residual strain of the gasket, the unloaded DAC may maintain a residual pressure above the ambient value. The 2D diffraction images were recorded at each pressure value. Also loaded into the sample chamber were small quantities of ruby ($\text{Cr-doped Al}_2\text{O}_3$) whose fluorescence signal was used to measure the applied hydrostatic pressure.

2.3. Unit-cell parameters analysis

Rietveld refinements of both the field and laboratory samples at ambient conditions were reported in our previous work (Geng *et al.*, 2020; Shi *et al.*, 2019), with the diffraction peaks well indexed. The raw diffraction images were integrated to the normal diffractogram using the *Dioplas* package (Prescher & Prakapenka, 2015). Here, instead of conducting Rietveld refinement of each sample at each pressure value, we followed the method used by Geng *et al.* (2018a). On each diffractogram, certain peak positions were determined using the *XFIT* package (Cheary & Coelho, 1996) assuming a pseudo-Voigt peak profile. Lattice parameters were then explicitly calculated according to the d -spacings of the tracked peaks, as described in detail in the results section. Complete

data of the d -spacings and the equations to calculate the lattice parameters are given in the supporting information.

3. Results

HP-XRD results of three field samples and a laboratory-synthesized sample are summarized as follows. The geometry of the unit cells are tracked as a function of the pressure, based on which the bulk moduli are calculated. The averaged bulk moduli at macroscale are then estimated as a function of the volume percentage of different phases and porosity.

3.1. HP-XRD of field samples

3.1.1. Mels_pore. Nine diffraction images were recorded for the sample Mels_pore. The first eight images were during the loading process from ambient pressure to 8.72 GPa, and the last was recorded after unloading to 1.98 GPa. Diffractograms were obtained from these images, as shown in Fig. 2(a). Based on our previous work (Geng *et al.*, 2020), peak indices are assigned and labeled here [Fig. 2(a)]. The basal peak (002) is clearly resolved throughout the studied pressure range and it generally moves to the high-angle side with increasing pressure. There is a clear change in its peak profile (width and intensity) from 0.96 GPa to 2.31 GPa, whereas the profile is consistent before 0.96 GPa and after 2.31 GPa. This profile change is accompanied by a drastic change in its peak position, as the (002) peak seems to abruptly drift to the position of the broad secondary basal peak [labeled by a black triangle in Fig. 2(a)]. In the meantime, a profile change is also observed for the strong diffraction at $1/d \sim 0.35\ \text{\AA}^{-1}$, where the (121) peak intensity overtakes the $(\bar{1}21)$ intensity when pressure is equal and above 2.31 GPa. These phenomena may indicate a phase change within the pressure range between 0.96 GPa and 2.31 GPa. Upon unloading to 1.98 GPa, the diffractogram shifted to the low-angle side, but the peak profiles remain similar to the profiles at higher pressure values.

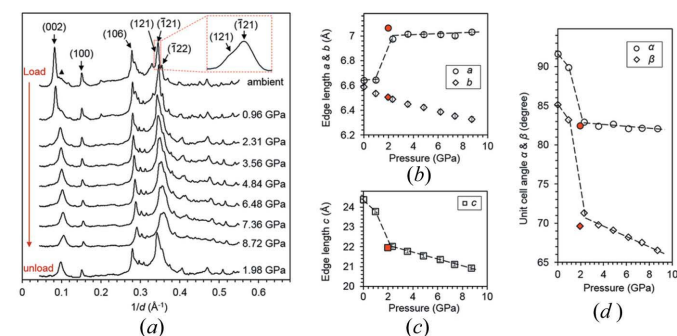


Figure 2

HP-XRD study of Mels_pore. (a) Diffractograms at different pressure values. The red-dashed inset is a magnification of the peak at $1/d \sim 0.35\ \text{\AA}^{-1}$. The calculated lattice parameters are shown in (b) edges a and b , (c) edge c and (d) angles α and β . The estimated uncertainty is indicated by error bars. The red-filled data points correspond to the unloaded condition. The dashed lines are guides for the eye when the data points follow discontinuous trend lines.

A previous study has confirmed the monoclinic structure of ASR product at ambient pressure, *i.e.* $\alpha = \gamma = 90^\circ$ (Geng *et al.*, 2020). The study also suggested that the structural variation of ASR product takes place by in-planar gliding between adjacent layers. Here in addition to β , the angle α is also subjected to re-calculation at each pressure value to account for the potential gliding along the a axis during the phase change. The d -spacings of (002), (100), (106), (121) and (122) are tracked at each pressure, and then used to solve the lattice parameters a , b , c , and angles α and β . Lists of peak positions and equations to solve the lattice parameters are available in the supporting information. These peaks were chosen because they are strong and isolated, and thus relatively easy to be track (Table S1).

The calculated lattice parameters are plotted in Figs. 2(b), 2(c) and 2(d). The edge length a is nearly constant at either the low-pressure range (≤ 0.96 GPa) or the high-pressure range (≥ 2.31 GPa). However, it undergoes a significant increase from 6.64 Å to 7.00 Å when pressure increases from 0.96 to 2.31 GPa. In contrast, parameter b decreases from 6.59 Å to 6.33 Å when pressure increases from ambient to 8.72 GPa, roughly following a linear trend. The parameter c also decreases with increasing pressure, and there is a clear drop when pressure increases from 0.96 to 2.31 GPa. Besides, the incompressibility of c seems to follow two trend lines with distinct slopes in the low-pressure and high-pressure ranges [dashed lines in Fig. 2(c)]. At the low-pressure range, c shortens faster when pressure increases, corresponding to a 'softer' behavior under compression, compared with the case at high-pressure range.

The angles α and β are calculated to be 91.5° and 85.1° at ambient pressure, in general consistence with the reported result from Rietveld refinement (Geng *et al.*, 2020) assuming a monoclinic structure (90° and 85.3° , respectively). The angle α rapidly decreases to 82.9° when pressure reaches 2.31 GPa and remains nearly constant at higher pressure values. Meanwhile, β rapidly drops to 71.3° at 2.31 GPa, and continues to drop at elevated pressure but at a lower rate ($\sim 0.8^\circ \text{ GPa}^{-1}$). The significant decrease of α and β indicates that the phase change between 0.96 and 2.31 GPa takes place via a layer glide along

both a and b axes, accompanied by a quick shortening of the interlayer spacing (*i.e.* a collapse). The high-pressure phase has a stiffer behavior along the c axis, compared with the ambient phase. When unloaded to 1.98 GPa, the lattice parameters generally remain on the trend line of the high-pressure data points [red-filled points in Figs. 2(b), 2(c) and 2(d)], instead of the low-pressure data points.

3.1.2. ES1_agg. Eight diffraction patterns from ambient pressure to 7.5 GPa and one diffraction pattern at unloading condition (1.65 GPa) were collected for ES1_agg [Fig. 3(a)]. The diffractograms of ES1_agg are generally similar to those of Mels_pore, except that multiple basal diffraction peaks are observed for ES1_agg. As shown in Fig. 3(b), at ambient pressure the dominating peak (002)_1 has a d -spacing of ~ 12.16 Å, which is comparable with the (002) peak of Mels_pore. Three more diffraction peaks are observed in the basal diffraction range, *i.e.* (002)_0, (002)_2 and (002)_3 [Fig. 3(b)]. This suggests that several crystalline phases with slightly different basal spacing are present in ES1_agg, and the phase that produces the (002)_1 peak is highly comparable to Mels_pore.

Upon applying external pressure, the (002)_1 peak remains dominant at 0.93 GPa, whereas it quickly vanishes upon further loading to 2.0 GPa. Meanwhile, the intensity of (002)_2 increases when (002)_1 vanishes, yet it splits into two peaks at elevated pressure, *i.e.* > 3.1 GPa. This is consistent with the observation in Mels_pore that the (002)_1 peak undergoes a sudden shift to the high-angle side [here, close to the position of peak (002)_2] when the applied pressure increases from 0.93 to above 2 GPa. The (002)_1 peak at the elevated pressure drifts at a different rate compared with the (002)_2 peak, thus resulting in their split at high-pressure values. The (002)_0 peak remains observed but with very low intensity throughout the studied pressure range. The (002)_3 peak is decreasingly resolved at elevated pressure.

In addition to the multiple basal peaks, the ES1_agg also exhibits doublet peaks for both the (100) and the (106)

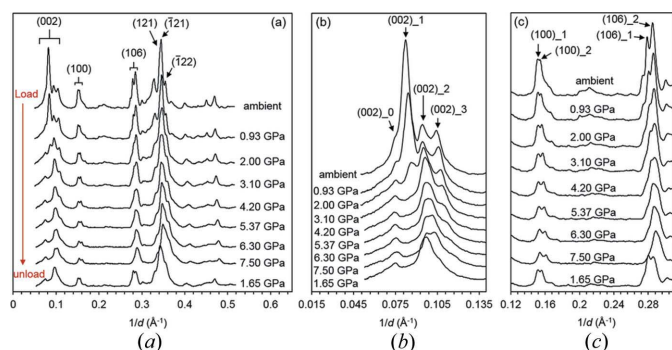


Figure 3
HP-XRD study of ES1_agg. (a) diffractograms at different pressure values; magnified diffractograms of (b) the multiple basal peaks, and (c) the (100) and (106) peaks. Peaks corresponding to different phases are indicated by the numbers after the Miller indices. For example, (100)_1 is the (100) diffraction of phase_1; (106)_2 is the (106) diffraction of phase_2.

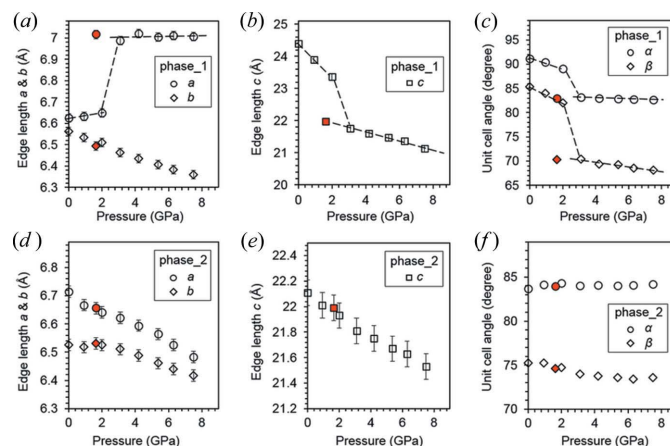


Figure 4
Calculated lattice parameters of ES1_agg as a function of the applied pressure: (a–c) phase_1 and (d–f) phase_2. The red-filled data points correspond to the unloaded condition. The dashed lines are guides for the eye when the data points follow discontinuous trend lines.

reflections [Fig. 3(c)]. The positions of (100)₁ and (106)₁ peaks are consistent with their counter parts in Mels_pore [Fig. 2(a)]. Therefore they are considered to belong to the phase that produces peak (002)₁. The peaks (100)₂ and (106)₂ are clearly resolved throughout the studied pressure range. Thus they most likely belong to the phases that produce (002)₂. No peak splitting is observed for the (121), (121) and (122) reflections in ES1_agg, suggesting that the multiple phases in ES1_agg produce nearly the same diffraction profile at this 2θ range ($1/d \sim 0.3\text{--}0.4 \text{ \AA}^{-1}$).

Following the above analysis, we are able to track the peak positions (*i.e.* $1/d$) that are assigned to the dominant phase (phase₁) and the secondary phase (phase₂) (Table S2). Based on the $1/d$ values measured at each pressure, the lattice parameters of phase₁ and phase₂ were calculated, as shown in Fig. 4. Phase₁ corresponds to the phase that produces the (002)₁, (100)₁ and (106)₁ reflections, and phase₂ corresponds to the phase that produces the (002)₂, (100)₂ and (106)₂ reflections. Phase₁ behaves nearly identically as the dominant phase in Mels_pore (Fig. 2). Upon loading beyond 2 GPa, the unit cell of phase₁ experiences a sudden increase in lattice parameter *a* [Fig. 4(a)], and a decrease in lattice parameter *c* [Fig. 4(b)] and the angles α and β [Fig. 4(c)]. Such a phenomenon suggests that phase₁ undergoes a phase change near 2 GPa. The phase change happens via a sudden glide between adjacent layers along both *a* and *b* axes, and is accompanied by a shortening of $\sim 1 \text{ \AA}$ in the interlayer spacing. Upon unloading to 1.65 GPa [red-filled data points in Figs. 4(a)–4(c)], the lattice parameters remain in the same trend lines of the high-pressure data points. This indicates that phase₁ remains the high-pressure polymorph when it is unloaded to 1.65 GPa.

Phase₂ in ES1_agg behaves distinctly compared with phase₁. At ambient conditions, the basal spacing and interaxial angles of phase₂ are similar to those of the high-pressure polymorph of phase₁ [Figs. 4(d)–4(f)]. Upon loading, the unit-cell edge lengths of phase₂ continuously decrease as the pressure increases, except that the lattice parameter *b* remains roughly unchanged below 2 GPa. The unit-cell angles α and β remain nearly unchanged within the studied pressure range. Throughout the loading period, no sudden change is observed

for the lattice parameters of phase₂. When unloaded to 1.65 GPa, the lattice parameters of phase₂ roughly return to the values that are in the same trend line as the data points of the loading process. This indicates that phase₂ is elastically compressed under hydrostatic load and does not experience any phase change.

3.1.3. ES1_pore. The HP-XRD results of ES1_pore are shown in Fig. 5. At ambient pressure, one dominant basal peak was observed for ES1_pore [Figs. 5(a) and 5(b)] with the same *d*-spacing as the dominant peak (002)₁ in ES1_agg. A secondary basal peak (002)₂ is clearly resolved, together with two weak and broad humps corresponding to the (002)₀ and (002)₃ peaks of ES1_agg [Fig. 5(b)]. The doublet peaks for (100) and (106) diffraction are also observed [Fig. 5(c)], suggesting that ES1_pore is also a mixture of several crystalline phases, similar to ES1_agg. Upon loading to 2.01 GPa, the (002)₁ peak drifts to the high-angle side and becomes much less intense compared to the ambient conditions [Fig. 5(b)]. Meanwhile the intensity of (002)₂ increases. At 4.03 GPa, the (002)₁ peak seems to completely merge with peak (002)₂, yet they split at higher pressure values [Fig. 5(b)].

Using the *d*-spacing values obtained from each diffractogram (see Table S3), the lattice parameters of ES1_pore as a function of pressure were calculated and plotted in Fig. 6, *i.e.* phase₁ [Figs. 6(a)–6(c)] and phase₂ [Figs. 6(d)–6(f)]. Phase₁ undergoes a phase change when loaded beyond 2 GPa. During this phase change, its lattice parameter *a* increases by $\sim 0.4 \text{ \AA}$ [Fig. 6(a)] while parameter *c* drops by $\sim 1 \text{ \AA}$ [Fig. 6(b)]. Its angle α drops to $\sim 84^\circ$ and β drops to $\sim 69^\circ$, from $\sim 91^\circ$ and $\sim 85^\circ$ at ambient conditions, respectively [Fig. 6(c)]. Phase₂ deforms more continuously by shortening its unit-cell edge lengths along all three axes [Figs. 6(d) and 6(e)], while maintaining a constant interaxial angle β at $\sim 75^\circ$ [Fig. 6(f)]. The angle α of phase₂ also decreases from 91° (ambient) to $\sim 83^\circ$ (beyond 4 GPa), which is different from the phase₂ in ES1_agg whose angle α remains $\sim 84^\circ$ throughout the loading.

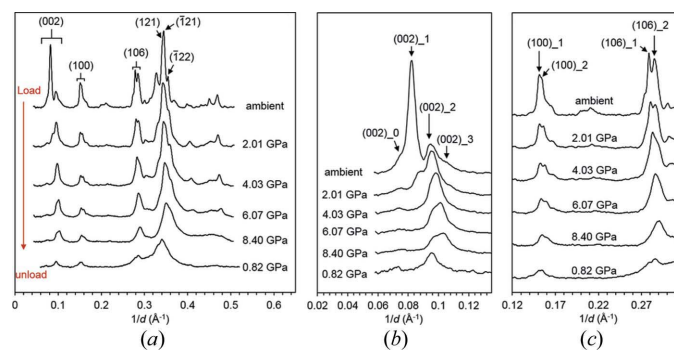


Figure 5
HP-XRD study of ES1_pore: (a) diffractograms at different pressure values, (b) magnified diffractograms of the multiple basal peaks and (c) the (100) and (106) peaks.

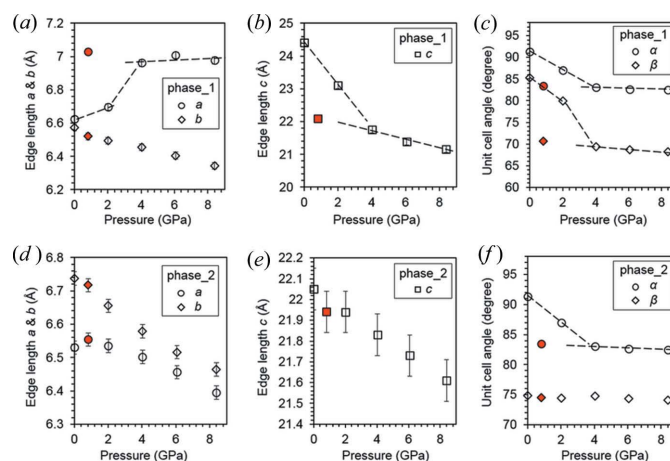


Figure 6
Calculated lattice parameters of ES1_pore as a function of the applied pressure: (a–c) phase₁ and (d–f) phase₂. The red-filled data points correspond to the unloaded condition. The dashed lines are guides for the eye when the data points follow discontinuous trend lines.

Upon unloading to 0.82 GPa [red-filled symbols in Figs. 6(a)–6(c)], phase_1 clearly maintains its high-pressure polymorph structure. Although phase_2 deforms more continuously during loading, its parameters c and α , when unloaded, seem to be on a different trend line of the loading process. For example, the α remains $\sim 83^\circ$ when unloaded to 0.82 GPa [Fig. 6(d)], suggesting a permanent layer-glide along the a axis. Note that such a glide modifies the phase_2 in ES1_pore to be the same as the phase_2 in ES1_agg.

3.2. HP-XRD of the laboratory-synthesized sample

The laboratory-synthesized sample SKC has a nearly identical main layer structure as the field ASR samples, yet the basal spacing of SKC (~ 13.3 Å) is larger than that of the dominant phase (phase_1) in the field samples (~ 12.2 Å). Our previous study suggested that the interlayer region of SKC is more structurally stable than that of the field samples, as indicated by the constant presence of one unique basal peak (002) [Fig. 7(a)]. This is probably due to the relatively high synthesis temperature (80°C) of laboratory samples (Shi *et al.*, 2019). Its diffractograms under changing pressure up to 7.36 GPa and under unloaded condition (1.60 GPa) are shown in Fig. 7(a). Throughout the pressure range, there is only one clearly resolved basal peak, which significantly broadens at elevated pressure. This is due to the pressure-induced structural disorder, which also leads to the occurrence of the broad background hump in the $1/d$ range between 0.25 and 0.4 Å $^{-1}$. Upon unloading to 1.60 GPa, the (002) peak regains its sharpness, suggesting a merely elastic deformation.

The diffraction peaks have been indexed using a shlykovite structure from our previous study (Shi *et al.*, 2019). The d -spacings of peaks (002), (100), (106), (121) and (025) were obtained (see Table S4) and used to calculate the lattice parameters at each pressure, as shown in Figs. 7(b)–7(d). The unit-cell edge lengths decrease continuously when pressure increases. However there seems to exist a change of the trend line when pressure increases from 2 to 3 GPa. The angle β slightly increases at the first pressure value (~ 1 GPa), whereas it decreases continuously when pressure is beyond 1 GPa. The

angle α remains nearly unchanged throughout the studied pressure range. Upon unloading, the lattice parameters fall on the trend line of loading [red filled symbols in Figs. 7(b)–7(d)]. These observations indicate that SKC undergoes elastic deformation when hydrostatically loaded to ~ 8 GPa.

3.3. Bulk modulus

The above results readily point to the metastable nature of the dominant phase (phase_1) in the studied field ASR samples. In all three field samples, phase_1 (with basal spacing of ~ 12.2 Å) undergoes a phase change when the applied pressure reaches ~ 2 GPa. The phase change takes place via a collapse of the interlayer opening (by ~ 1 Å), accompanied by an in-planar glide of the adjacent main layers, such that the angle α decreases by $5 \pm 2^\circ$ and angle β decreases by $10 \pm 2^\circ$. After unloading to 0.82 GPa, phase_1 still remains the structure of the high-pressure polymorph, indicating that it might be more stable compared with the low-pressure polymorph. Considering the possibility of a hysteresis in the phase change, a confirmation of this finding would require unloading the high-pressure polymorph completely to the ambient conditions (~ 0 GPa) or to apply thermal activation by heating the high-pressure polymorph. These unfortunately are not provided in the current study.

Both the laboratory-synthesized SKC and phase_2 in the field sample are stable within the studied pressure range. Despite the a -glide observed for phase_2 in ES1_pore, the deformation of phase_2 and SKC under compression are generally elastic and their unit cells return to the original geometry upon unloading.

Using the calculated lattice parameters, the unit-cell volumes of the above phases were obtained and plotted as a function of applied pressure (Fig. 8). The results of the dominant phase (phase_1) in Mels_pore, ES1_agg and ES1_pore are combined in Fig. 8(a); results of phase_2 in ES1_agg and ES1_pore are combined in Fig. 8(b). The phase change of phase_1 at ~ 2 GPa is again confirmed in Fig. 8(a) by the two distinct trend lines for the low-pressure polymorph (upper half of the plot) and the high-pressure polymorph (lower half of the plot). The accompanied change of interlayer spacing and the in-planar glide are also illustrated in Fig. 8(a). The volume-pressure trend lines for phase_2 and SKC [Fig. 8(b)] are continuous over the whole pressure range, suggesting that there is no phase change for these phases.

The bulk moduli are estimated by fitting the volume–pressure data with the second-order Birch–Murnaghan equation of state [equation (1)] (Birch, 1952):

$$P = \frac{3}{2} K_0 \left[\left(\frac{V}{V_0} \right)^{\frac{7}{3}} - \left(\frac{V}{V_0} \right)^{\frac{5}{3}} \right], \quad (1)$$

where V_0 is the unit-cell volume at ambient pressure; V is the unit-cell volume at pressure P ; K_0 is the bulk modulus at ambient pressure. The bulk moduli of the low- and high-pressure polymorphs of phase_1 are 27 ± 3 and 46 ± 3 GPa, respectively. A bulk modulus of 76 ± 4 GPa is obtained for phase_2 and of 35 ± 2 GPa for SKC.

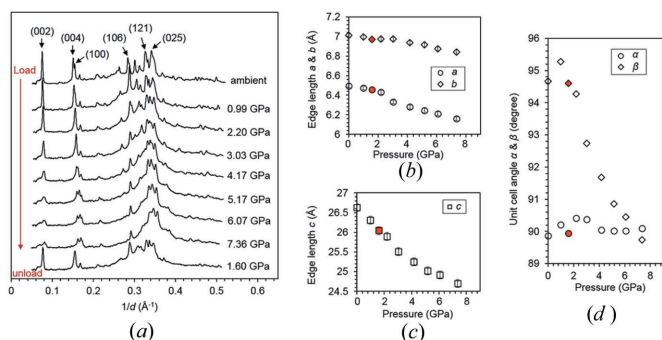


Figure 7
HP-XRD study of SKC. (a) Diffractograms at different pressure. The calculated lattice parameters are shown in (b) edges a and b , (c) edge c and (d) angles α and β . The red filled data points correspond to the unloaded condition.

At ambient conditions, the crystalline ASR product veins in the studied samples are dominated by the low-pressure polymorph of phase_1, with a minor content of phase_2. Therefore, the variation of their volume ratio, together with the porosity (gaps between nano-platelets, Fig. 1), determines the average bulk modulus (K_{average}) of the product at macro-scale. The geometric information and the orientation of the ASR crystals are needed to perform a precise prediction of K_{average} , similar to what has been reported for C-S-H (Geng *et al.*, 2018b), particularly when the crystal has anisotropic mechanical behavior (Vasin *et al.*, 2013). However considering the general rule of mixing (Li & Wang, 2008), an upper and lower bound can be readily determined for K_{average} . They are calculated based on the Voigt [equation (2)] and Reuss [equation (3)] assumption, respectively (Li & Wang, 2008).

$$\text{Upper bound : } K_{\text{average}} = \sum_i f_i K_i \quad (2)$$

$$\text{Lower bound : } K_{\text{average}} = 1 / \sum_i \left(\frac{f_i}{K_i} \right) \quad (3)$$

The f_i is the volume percentage and K_i is the bulk modulus of each phase. The considered phases here are ASR product

phase_1 (low-pressure polymorph) and phase_2, and water that fills the porosity [bulk modulus ~ 2.2 GPa (Fine & Millero, 1973)]. The calculated K_{average} values are plotted in Figs. 8(c) and 8(d). In the range of 0 to 1, the volume ratio of phase_2 over phase_1 (V_2/V_1) does not affect K_{average} significantly, especially in the case of large porosity. At zero porosity, the difference between the lower and upper bounds is small. K_{average} ranges between 27 and 35 GPa when V_2/V_1 ranges from 0 to 1. When porosity ranges from 0.2 to 0.6, the lower bound of K_{average} is usually below 10 GPa, whereas its upper bound ranges from ~ 15 to ~ 30 GPa [Fig. 8(c)]. At fixed $V_2/V_1 = 0.5$, when the porosity reaches 0.8, K_{average} has lower and upper bounds of ~ 3 and ~ 8 GPa, respectively [Fig. 8(d)].

4. Discussion and conclusions

The major phases (phase_1) from sources ES1 and Mels are identical because they follow the same P - V trend lines in both low-pressure and high-pressure ranges [Fig. 8(a)]. The investigation of three field samples suggests that the presence of multiple phases is likely to be universal in ASR-affected concrete. Although these phases share the same main layer structure, they exhibit different stacking patterns between adjacent layers (Geng *et al.*, 2020). Such a difference results in different mechanical response under compression. For example, phase_1 undergoes permanent shear-gliding when pressure is above ~ 2 GPa, accompanied by an drastic increase of bulk modulus from 27 ± 3 to 46 ± 3 GPa. Phase_2 already has a smaller basal spacing and smaller β angle than phase_1 at ambient conditions. Therefore under compression, it exhibits a much higher bulk modulus (76 ± 4 GPa) and no sign of phase change.

Note that two other phases are observed in ES1_agg, corresponding to the minor basal peak (002)_0 and (002)_3 [Fig. 3(b)]. Their structural evolution under pressure could not be tracked due to their minimal contents and the absence of basal peaks at elevated pressure. Nonetheless, their presence, again, demonstrates the multiphase nature of real crystalline ASR product. In contrast, the laboratory-synthesized sample (SKC) exhibits a unique basal peak and also no sign of phase change under compression. A possible explanation to this phenomenon could be the 'jagged' surface of the main layer, where two silicate tetrahedra, out of every eight-membered silicate ring, significantly stretch into the interlayer region (Fig. 1). When the adjacent main layers glide parallel to each other, this unevenness may result in several energy barriers and thus multiple metastable orientations that have locally minimum energy. Similar phenomena have also been reported for calcium chain-silicate structures, *e.g.* C-S-H (Morshedifard *et al.*, 2018; Masoumi *et al.*, 2017). When high temperature (*e.g.* for the synthesis of SKC) or pressure is applied, the system may overcome the local energy barriers and reach a configuration with global minimum energy.

The bulk modulus of each ASR product phase is precisely calculated using the HP-XRD data. The estimation of the macroscale K_{average} , however, depends strongly on the

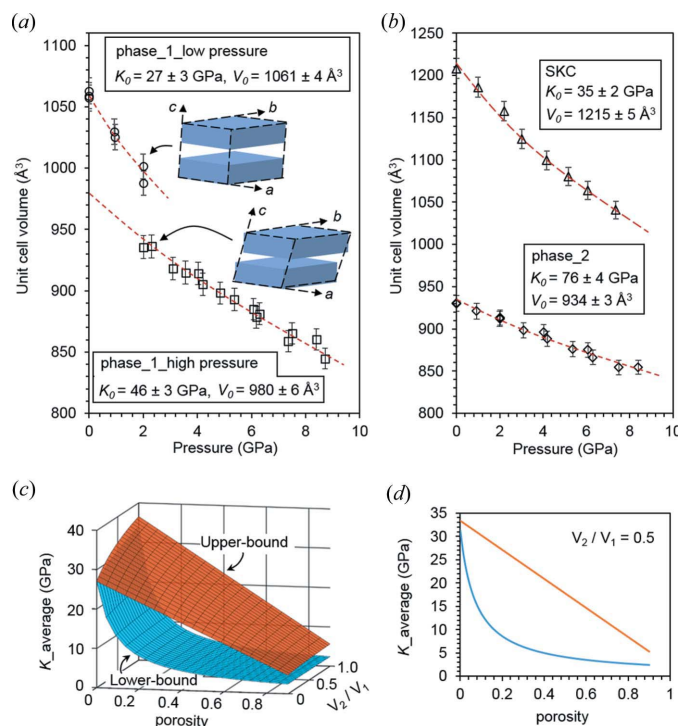


Figure 8

The unit-cell volume as a function of applied hydrostatic pressure, (a) low-pressure (circle) and high-pressure (square) polymorphs of phase_1, (b) phase_2 (diamond) and SKC (triangle). The red dashed curves are guides for the eye. The fitted bulk modulus (K_0) and ambient unit-cell volume (V_0) are given. The upper and lower bounds of the average bulk modulus are plotted in (c) as a function of porosity and phase_2 to phase_1 volume ratio (V_2/V_1). Note that V_2/V_1 varies from 0 to 1 in the calculation to maintain phase_1 as the major phase. Plot (d) is a cross-section of (c) when $V_2/V_1 = 0.5$.

porosity inside the crystalline ASR product vein, and to a lower extent on the volume ratio of phase_1 and phase_2. This is consistent with the scatter in the reported K_{average} from nano-indentation measurements. It seems that a significant amount of porosity between nano-crystals is present at an indentation depth of $\sim 2\ \mu\text{m}$, as an elastic modulus $< 15\ \text{GPa}$ has been obtained (Leemann & Lura, 2013; Zhang *et al.*, 2017), corresponding to a bulk modulus $< 10\ \text{GPa}$ assuming a Poisson's ratio of 0.25. A much larger elastic modulus was obtained (*i.e.* $\sim 65\ \text{GPa}$) when the indentation depth is $< 0.5\ \mu\text{m}$ (Hu *et al.*, 2018), corresponding to a bulk modulus of $\sim 43\ \text{GPa}$ (near the upper bound of K_{average} at zero porosity).

The pressure at the tip of the indenter is in the order of several GPa. As demonstrated by this study, the most abundant crystalline ASR product (phase_1) may undergo phase change at such a high pressure. Depending on the stress distribution within the interaction volume near the indenter tip, nano-indentation may always be measuring a mixed volume of both low-pressure and high-pressure polymorphs of phase_1, as well as a minor content of phase_2. Therefore, even taking the porosity into account, nano-indentation may not be able to precisely probe the mechanical property of ASR product at ambient conditions. Since the high-pressure polymorph of phase_1 is 70% stiffer than its low-pressure polymorph, the elastic modulus measured by nano-indentation might be slightly larger than the real elastic modulus at ambient conditions. Again, the deviation depends on porosity and volume percentage of phase_1.

We hereby summarize our findings as the following.

(1) ASR products extracted from veins in affected structure contain multiple phases. These phases have similar main layer structure, but differ in the spacing and stacking orientation between adjacent layers.

(2) The dominant phase in the studied field samples has a bulk modulus of $27 \pm 3\ \text{GPa}$. It undergoes a phase change at $\sim 2\ \text{GPa}$ to a high-pressure polymorph with a bulk modulus of $46 \pm 3\ \text{GPa}$. The phases change takes place via a shortening of $\sim 1\ \text{\AA}$ in the interlayer spacing, accompanied by a shear glide of the main layer along both a and b axes. This phase change is not reversible when unloaded to $\sim 0.8\ \text{GPa}$.

(3) The minor phase in the studied field samples has a bulk modulus of $76 \pm 4\ \text{GPa}$. It exhibits no phase change during compression to $\sim 8\ \text{GPa}$. The laboratory-synthesized ASR product (SKC) has a bulk modulus of $35 \pm 2\ \text{GPa}$, and also undergoes no phase change during compression. Both SKC and the minor phase in field samples are thus more structurally stable than the dominant phase in field samples.

(4) The presence of several phases with different bulk moduli in field ASR samples and the strong dependence on the porosity are consistent with the large range of elastic moduli obtained from indentation measurements.

Acknowledgements

We acknowledge DESY (Hamburg, Germany), a member of the Helmholtz Association HGF, for the provision of experi-

mental facilities at beamline P02.2. We also acknowledge Diamond Light Source for providing beamtime at beamline I15 under Proposal EE18643.

Funding information

This project is funded by the SNF Sinergia project: Alkali-silica reaction in concrete (ASR), grant number CRSII5_17108. G. Geng acknowledges the funding from European Union's Horizon 2020 research and innovation programme under the Marie Skłodowska-Curie grant agreement number 701647. Z. Shi acknowledges the EMPA-POSTDOCS-II programme funded by the European Union's Horizon 2020 research and innovation programme under the Marie Skłodowska-Curie grant agreement number 754364.

References

- Birch, F. (1952). *J. Geophys. Res.* **57**, 227–286.
- Cheary, R. W. & Coelho, A. A. (1996). *XFIT*. Engineering and Physical Sciences Research Council, Daresbury Laboratory, <http://www.CCP14.ac.uk/tutorial/xfit-95/xfit.htm>.
- Cole, W. F., Lancucki, C. J. & Sandy, M. J. (1981). *Cem. Concr. Res.* **11**, 443–454.
- Comboni, D., Gatta, G. D., Lotti, P., Merlini, M. & Hanfland, M. (2019). *Cem. Concr. Res.* **120**, 46–51.
- Constantinides, G. & Ulm, F. J. (2007). *J. Mech. Phys. Solids*, **55**, 64–90.
- Dähn, R., Arakcheeva, A., Schaub, P., Pattison, P., Chapuis, G., Grolimund, D., Wieland, E. & Leemann, A. (2016). *Cem. Concr. Res.* **79**, 49–56.
- De Ceukelaire, L. (1991). *Mater. Struct.* **24**, 169–171.
- Fernández-Jiménez, A. & Puertas, F. (2002). *Cem. Concr. Res.* **32**, 1019–1024.
- Fine, R. A. & Millero, F. J. (1973). *J. Chem. Phys.* **59**, 5529–5536.
- Fournier, B. & Bérubé, M. A. (2000). *Can. J. Civ. Eng.* **27**, 167–191.
- Geng, G., Li, J., Zhou, Y., Liu, L., Yan, J., Kunz, M. & Monteiro, P. J. (2018a). *Cem. Concr. Res.* **108**, 38–45.
- Geng, G., Myers, R. J., Li, J., Maboudian, R., Carraro, C., Shapiro, D. A. & Monteiro, P. J. (2017a). *Sci. Rep.* **7**, 44032.
- Geng, G., Myers, R. J., Qomi, M. J. A. & Monteiro, P. J. (2017b). *Sci. Rep.* **7**, 10986.
- Geng, G., Shi, Z., Leemann, A., Borca, C., Huthwelker, T., Glazyrin, K., Pekov, I. V., Churakov, S., Lothenbach, B., Dähn, R. & Wieland, E. (2020). *Cem. Concr. Res.* **129**, 105958.
- Geng, G., Vasin, R. N., Li, J., Qomi, M. J. A., Yan, J., Wenk, H. R. & Monteiro, P. J. (2018b). *Cem. Concr. Res.* **113**, 186–196.
- Hou, X., Struble, L. J. & Kirkpatrick, R. J. (2004). *Cem. Concr. Res.* **34**, 1683–1696.
- Hu, C., Gautam, B. P. & Panesar, D. K. (2018). *Constr. Build. Mater.* **158**, 75–83.
- Hu, Z., Hilaire, A., Ston, J., Wyrzykowski, M., Lura, P. & Scrivener, K. (2019). *Cem. Concr. Res.* **121**, 11–20.
- Iskhakov, T., Timothy, J. J. & Meschke, G. (2018). In *Computational Modelling of Concrete Structures. Proceedings of the Conference on Computational Modelling of Concrete and Concrete Structures (EURO-C 2018)*, 26 February–1 March 2018, Bad Hofgastein, Austria. CRC Press.
- Johnson, C. V., Chen, J., Hasparyk, N. P., Monteiro, P. J. & Akono, A. T. (2017). *Cem. Concr. Compos.* **79**, 71–75.
- Katayama, T. (2012). *Proceedings of the 14th International Conference on Alkali-Aggregate Reaction (ICAAR)*, 20–25 May 2012, Austin, Texas, USA.
- Leemann, A. (2017). *Cem. Concr. Res.* **102**, 41–47.

- Leemann, A., Le Saout, G., Winnefeld, F., Rentsch, D. & Lothenbach, B. (2011). *J. Am. Ceram. Soc.* **94**, 1243–1249.
- Leemann, A. & Lura, P. (2013). *Constr. Build. Mater.* **44**, 221–227.
- Li, S. & Wang, G. (2008). *Introduction to Micromechanics and Nanomechanics*. Singapore: World Scientific Publishing Company.
- Mao, H. K., Xu, J. A. & Bell, P. M. (1986). *J. Geophys. Res.* **91**, 4673–4676.
- Masoumi, S., Valipour, H. & Abdolhosseini Qomi, M. J. (2017). *J. Phys. Chem. C*, **121**, 5565–5572.
- Mehta, P. K. & Monteiro, P. J. (2014). *Concrete Microstructure, Properties, and Materials*, 4th ed. New York: McGraw-Hill Companies.
- Moon, J., Oh, J. E., Balonis, M., Glasser, F. P., Clark, S. M. & Monteiro, P. J. (2012). *Cem. Concr. Res.* **42**, 105–110.
- Moon, J., Speziale, S., Meral, C., Kalkan, B., Clark, S. M. & Monteiro, P. J. (2013). *Cem. Concr. Res.* **54**, 55–60.
- Morshedifard, A., Masoumi, S. & Abdolhosseini Qomi, M. J. (2018). *Nat. Commun.* **9**, 1785.
- Pekov, I. V., Zubkova, N. V., Filinchuk, Y. E., Chukanov, N. V., Zadov, A. E., Pushcharovsky, D. Y. & Gobechiya, E. R. (2010). *Geol. Ore Deposit.* **52**, 767–777.
- Peterson, K., Gress, D., Van Dam, T. & Sutter, L. (2006). *Cem. Concr. Res.* **36**, 1523–1532.
- Prescher, C. & Prakapenka, V. B. (2015). *High Pressure Res.* **35**, 223–230.
- Prezzi, M., Monteiro, P. J. & Sposito, G. (1997). *ACI Mater. J.* **94**, 10–17.
- Rajabipour, F., Giannini, E., Dunant, C., Ideker, J. H. & Thomas, M. D. (2015). *Cem. Concr. Res.* **76**, 130–146.
- Shi, Z., Geng, G., Leemann, A. & Lothenbach, B. (2019). *Cem. Concr. Res.* **121**, 58–71.
- Shi, Z., Leemann, A., Rentsch, D. & Lothenbach, B. (2020). *Mater. Des.* **190**, 108562.
- Shi, Z. & Lothenbach, B. (2019). *Cem. Concr. Res.* **126**, 105898.
- Shi, Z., Shi, C., Zhao, R. & Wan, S. (2015). *Mater. Struct.* **48**, 743–751.
- Thomas, M. (2001). *Materials Science in Concrete. Calcium Hydroxide in Concrete*, edited by J. P. Skalny, J. Gebauer and I. Odler, pp. 225–236.
- Vasin, R. N., Wenk, H. R., Kanitpanyacharoen, W., Matthies, S. & Wirth, R. (2013). *J. Geophys. Res. Solid Earth*, **118**, 3931–3956.
- Zhang, C., Sorelli, L., Fournier, B., Duchesne, J., Bastien, J. & Chen, Z. (2017). *Constr. Build. Mater.* **148**, 455–464.
- Zhou, Y., Orozco, C. A., Duque-Redondo, E., Manzano, H., Geng, G., Feng, P., Monteiro, P. J. & Miao, C. (2019). *Cem. Concr. Res.* **115**, 20–30.